Title

Probing Heterogeneous Degradation of Catalyst in PEM Fuel Cells under Realistic Automotive Conditions with Multi-Modal Techniques

Journal

Advanced Energy Materials, 11(35)

ISSN

1614-6832

Authors

Khedekar, Kaustubh

Talarposhti, Morteza Rezaei

Besli, Münir M

et al.

Publication Date

2021-09-01

DOI

10.1002/aenm.202101794

Peer reviewed

TESCAN

TESCAN micro-CT solutions for energy storage materials research

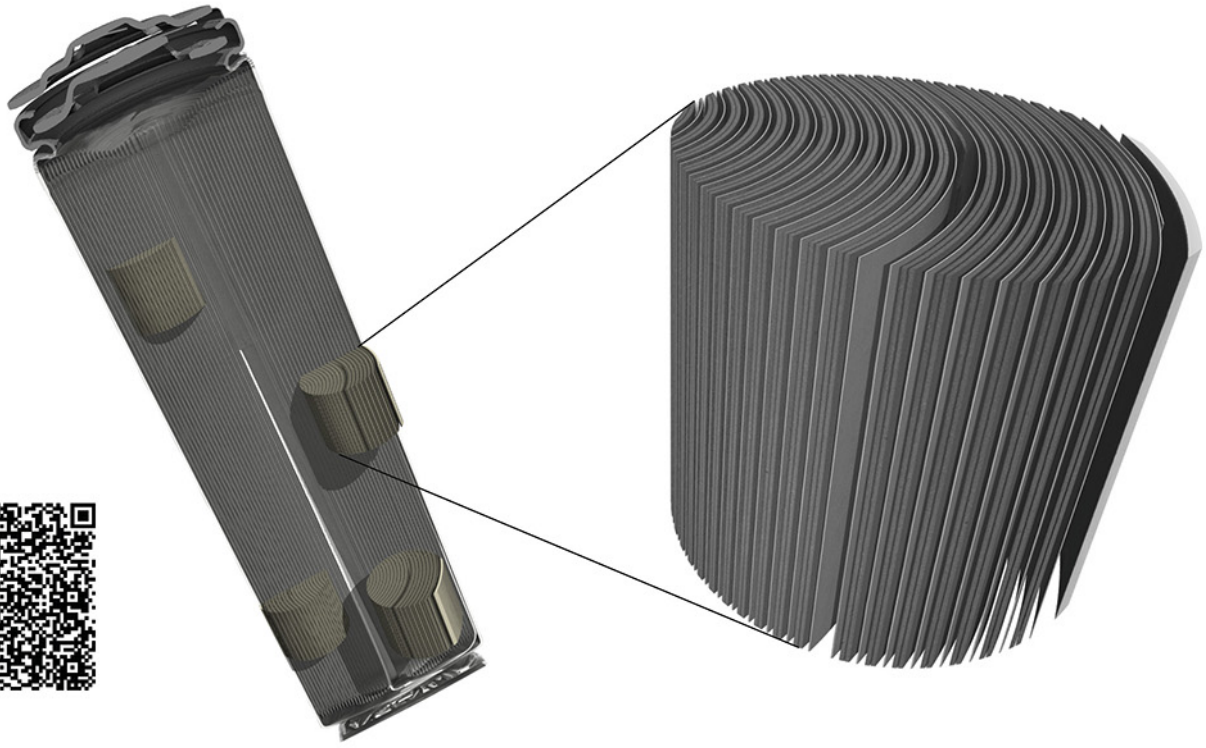

TESCAN UniTOM XL

- ✓ Multi-scale non-destructive 3D imaging optimized to maximize throughput and contrast
- ✓ Fast scanning and high sample throughput with temporal resolutions below 10 seconds
- ✓ Wide array of samples types
- ✓ Enables dynamic tomography and *in-situ* experiments
- ✓ Dynamic screening for synchrotron beamtime
- ✓ Modular and open system with unmatched flexibility for research

Click and find out more

ADVANCED ENERGY MATERIALS
www.advenergymat.de

Probing Heterogeneous Degradation of Catalyst in PEM Fuel Cells under Realistic Automotive Conditions with Multi-Modal Techniques

Kaustubh Khedekar, Morteza Rezaei Talarposhti, Münir M. Besli, Saravanan Kuppan, Andrea Perego, Yechuan Chen, Michael Metzger, Sarah Stewart, Plamen Atanassov, Nobumichi Tamura, Nathan Craig, Lei Cheng, Christina M. Johnston,* and Iryna V. Zenyuk**

The heterogeneity of polymer electrolyte fuel cell catalyst degradation is studied under varied relative humidity and types of feed gas. Accelerated stress tests (ASTs) are performed on four membrane electrode assemblies (MEAs) under wet and dry conditions in an air or nitrogen environment for 30 000 square voltage cycles. The largest electrochemically active area loss is observed for MEA under wet conditions in a nitrogen gas environment AST due to constant upper potential limit of 0.95 V and significant water content. The mean Pt particle size is larger for the ASTs under wet conditions compared to dry conditions, and the Pt particle size under land is generally larger than under the channel. Observations from ASTs in both conditions and gas environments indicate that water content promotes Pt particle size growth. ASTs under wet conditions and an air environment show the largest difference in Pt particle size growth for inlet versus outlet and channel versus land, which can be attributed to larger water content at outlet and under land compared to inlet and under channel. From X-ray fluorescence experiments Pt particle size increase is a local phenomenon as Pt loading remains relatively uniform across the MEA.

1. Introduction

Polymer electrolyte fuel cell (PEFC) technology has advanced to reach the commercialization stage with more automotive manufacturers announcing new PEFC-based light and heavy-duty vehicles.[1] However, the durability and cost of such systems still remain a challenge.[2,3] Using the Department of Energy (DOE) cost-breakdown for the 80-kW_{net} stack for light-duty vehicles, the cost of precious metal electrocatalyst remains almost unchanged as production rate increases to 0.5 M PEFC stacks per year.[4] The cost of the electrocatalyst amounts to 31% of stack cost, for 0.5 M systems per year production rate.[4] Platinum (Pt) or Pt-alloys are used as electrocatalyst for the oxygen reduction reaction (ORR) on the cathode side and the hydrogen oxidation reaction on the anode side of PEFCs. Pt or Pt-alloy electrocatalysts are dispersed as nanoparticles onto carbon-black support. DOE has set a target of reducing Pt loading to 0.125 mg cm^{-2} to achieve the goal of \$12.6 kW_{net}^{-1} for a stack with power density target of 1.8 W cm^{-2}. Membrane electrode assemblies (MEAs) with lower catalyst loading are less durable,[1] thus, the cost issue cannot be resolved without focusing on the catalyst durability issue of the PEFC stack. Moreover, heavy-duty trucks (HDTs) require stacks with 25 000–30 000 h lifetime, which to date requires ≥0.4 mg cm^{-2}[70] Pt catalyst loading. Significant progress in

K. Khedekar, P. Atanassov, I. V. Zenyuk
Department of Material Science and Engineering
National Fuel Cell Research Center
University of California
Irvine, CA 92697, USA
E-mail: iryna.zenyuk@uci.edu

M. Rezaei Talarposhti, A. Perego, Y. Chen, P. Atanassov, I. V. Zenyuk
Department of Chemical and Biomolecular Engineering
National Fuel Cell Research Center
University of California
Irvine, CA 92697, USA

The ORCID identification number(s) for the author(s) of this article can be found under https://doi.org/10.1002/aenm.202101794.

DOI: 10.1002/aenm.202101794

M. M. Besli
Department of Mechanical Engineering
Karlsruhe Institute of Technology
76021 Karlsruhe, Germany

S. Kuppan, M. Metzger, S. Stewart, N. Craig, L. Cheng, C. M. Johnston
Bosch Research and Technology Center North America
Sunnyvale, CA 94085, USA
E-mail: lei.cheng2@us.bosch.com; christina.johnston@us.bosch.com

N. Tamura
Advanced Light Source
Lawrence Berkeley National Laboratory
Berkeley, CA 94720, USA

understanding and mitigating cathode catalyst degradation will be required to enable the ultimate 2050 HDT target of 0.25 mg cm^{-2} catalyst loading.

More generally, catalyst degradation occurring during PEFC operation impacts the performance by decreasing the power density of the stack and by increasing fuel consumption per generated kWh.[5,6] PEFC catalyst durability has been previously studied extensively.[7–11] Platinum electrocatalysts are more prone to degradation on the cathode side of the PEFCs, rather than the anode due to higher potentials and more oxidizing conditions.[12,13] Previously, Wang et al.[14] reported electrochemically active surface area (ECSA) loss of 54.5% and 30.2% for cathode and anode, respectively. They reported higher degradation rates (more ECSA loss) on the cathode side which is due to several factors including: i) wider range of potential, ii) higher difference in pH values, and iii) higher water content.

Previous study has shown that load changing and startup-shutdown, contribute the most to the overall performance degradation.[15] Dynamic load change is the largest contributor to degradation for various reasons: i) it induces humidity and thermal cycling, ii) it may cause gas starvation, and iii) potential cycling due to dynamic load degrades the Pt electrocatalyst. The basic metrics for the degradation evaluation are polarization curves and ECSA loss. Pt degradation and ECSA loss occur mainly through three mechanisms: Pt dissolution, Ostwald ripening, and Pt agglomeration.[16] Pt dissolution occurs at high potentials during both anodic and cathodic sweeps of potential cycling[17,18] and is a function of particle size and oxide coverage.[19] According to Gibbs–Thomson equation, smaller particles are more susceptible to dissolution (due to the inverse dependency of surface energy with particle size) and Pt ions are more likely to redeposit onto larger particles to induce Ostwald ripening.[20] For this to happen, both particles have to be electrically connected (carbon support) and have ionically conductive pathways for Pt^{2+} ions to transport. Ostwald ripening is slower for uniform particle sizes. High water content in catalyst layer intensifies electrochemical Ostwald ripening by providing ionic conductivity pathways through thin water films and by enhancing ionic conductivity of ionomer.

To assess PEFC durability, accelerated stress tests (ASTs) are used because the experimental time can be reduced compared to using a real vehicle drive-cycle, that typically (according to DOE durability targets[21]) needs to last 6000, 25 000, or 40 000 h for automotive, buses/HDTs, and stationary applications, respectively. ASTs generally include potential cycling between two potentials to simulate load change and accelerate degradation of the catalyst layer.[22–24] Degradation includes morphological changes in the catalyst layer that cause performance loss, such as crack formation, thickness loss, ECSA loss, and diffusive, ionic, and electric pathway connectivity loss leading to transport losses.[25,26] Degradation of PEFC has been both physically modeled[19] and experimentally investigated.[27] The influence of voltage cycle profiles on degradation of MEAs has been comprehensively reported by Stariha et al.[28] That study used square wave and triangular wave potential cycling and evaluated degradations of both the catalyst and the support in different potential ranges. ASTs with square wave voltage cycling showed the highest rate of catalyst degradation. This is since degradation rates, including ECSA loss, increase with the increase of dwell time at the upper potential limit (UPL).[29] The strong effect of the UPL dwell time in H_2/N_2 environment on the catalyst durability is attributed to the formation of a larger amount of Pt oxide, which results in higher Pt dissolution rates.[30–32]

Repeated oxidation and reduction of the Pt nanoparticle surface leads to dissolution of Pt, which is a primary mechanism of catalyst degradation.[20] The dissolution of Pt leads to two different ECSA loss pathways. In the first pathway, Pt ions redeposit on nearby larger Pt nanoparticles, thereby increasing the Pt nanoparticle size.[33] This is known as electrochemical Ostwald ripening. In the second pathway, Pt ions diffuse through the ionomer phase towards the membrane and are reduced in the membrane by the crossover hydrogen, which results in a Pt band formation at the membrane-cathode interface.[33,34] **Figure 1** shows the schematic of the AST potential cycle with the possible Pt degradation reaction mechanisms considered in this study. During the anodic scan (from low to high potential), pristine Pt surface is present (at beginning of test) at the lower potential limit (LPL). During the potential step from the LPL to the UPL[35] Pt dissolution occurs at the defect sites at a low rate. As the potential crosses 0.8 V, OH groups adsorb on the Pt surface ultimately leading to the formation of PtO, as the potential reaches the UPL.[36] During the potential hold at the UPL, PtO coverage increases, and a place-exchange mechanism may occur (where Pt and O exchange the position) along with Pt dissolution at a low rate.[35,37] As the potential is swept down to the LPL in the cathodic scan, PtO is reduced (≈0.8 V), as it reacts with protons to form dissolved Pt and water. If the LPL is in a low re-deposition potential range (above ≈0.6 V), then unavailability of pristine Pt surface for the Pt ions to redeposit can primarily lead to Pt band formation in the membrane with relatively low Pt particle size growth. If the LPL is in high re-deposition potential range (at or below ≈0.6 V), then the availability of pristine Pt surface for the Pt ions to redeposit can make Ostwald ripening as the primary ECSA loss pathway with higher Pt particle size growth. This also indicates that the amount of PtO formed during the UPL hold of AST cycles directly depends on the LPL (i.e., the availability of pristine Pt surface).[23,38] At lower UPLs, PtO coverage is lower, resulting in a smaller number of Pt ions formed, consequently causing less degradation over the AST duration.[31]

The degradation of the PEFC materials is a heterogeneous process due to the land-channel geometry of the flow-field, and non-uniform distribution of reactant gases in the catalyst layer under land and channel, as well as, inlet and outlet.[39] The inhomogeneity in the reactant distribution also creates non-uniform relative humidity (RH) and temperature distribution, where heat due to ORR is the largest contributor to the overall heat generation at high current density.[40] Local hot spots in the catalyst layer lead to membrane and catalyst layer degradation.[6] Heterogeneity of distribution of fuel in the catalyst layer causes hydrogen starvation in some regions of the cell resulting in higher degradation rates.[41]

General characterization tools for the catalyst layer degradation include in situ and post-mortem techniques. In situ, during the cell operation, the catalyst layer degradation can be analyzed with electrochemical techniques, such as ECSA measurements,[42,43] hydrogen crossover determination through linear sweep voltammetry (LSV),[44] and polarization resistance characterization through electrochemical impedance spectrometry

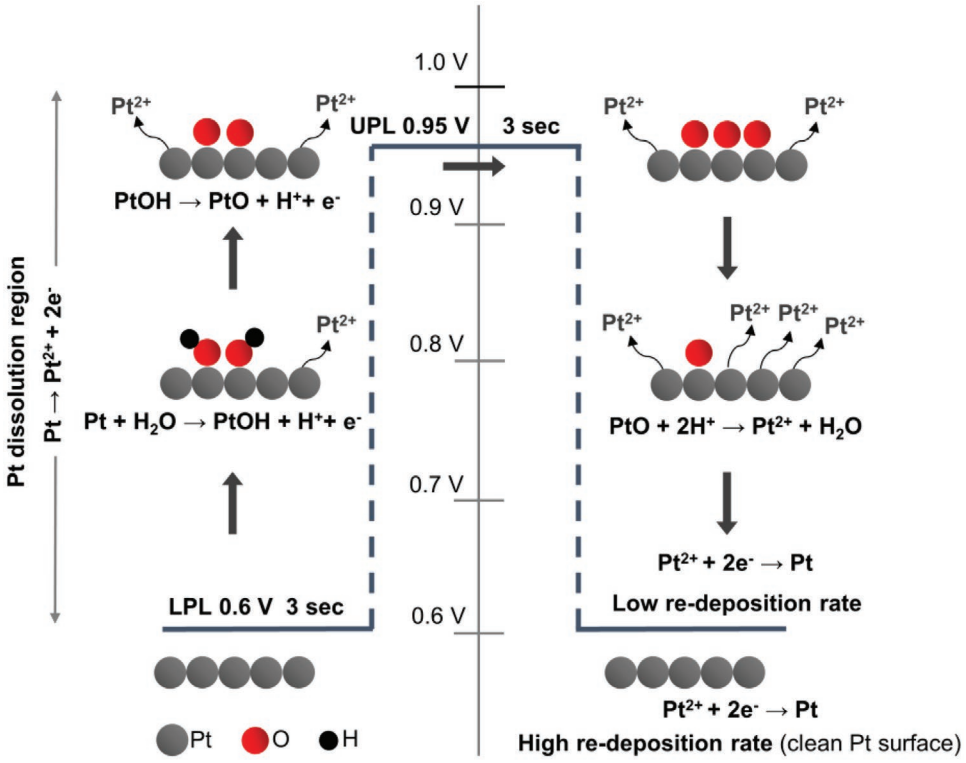

Figure 1. A schematic of the square wave AST potential profile used in this study and associated Pt degradation reaction mechanisms.

(EIS).[45,46] Imaging post-mortem techniques include SEM and transmission electron microscopy (TEM) for morphology investigation and particle size, elemental distribution analysis of a cross-section of an MEA.[47,48,49] In addition, 3D imaging techniques, such as X-ray computer tomography (X-ray CT) have been used to provide information about heterogeneous degradation, adding time as a fourth dimension.[50]

Our earlier work demonstrated for the first time, the use of synchrotron micro-X-ray diffraction (XRD) technique to map Pt particle size growth and distribution post-mortem for MEA aged in H_2/air environment under wet conditions.[51] The novel use of micro-XRD technique also identified heterogenous Pt particle size growth under land-channel geometry. The current study builds upon the previous study and investigates in detail the causes of heterogeneous Pt catalyst degradation rates by comparing ASTs in H_2/N_2 and H_2/air environments under wet and dry conditions. The effect of land and channel is further investigated using the same US DRIVE fuel cell tech team (FCTT) adopted AST protocols. A combination of electrochemical characterization and post-mortem characterization techniques (SEM/energy dispersive X-ray spectroscopy (EDS), micro XRD, X-ray CT, micro-X-ray fluorescence (micro XRF), X-ray photoelectron spectroscopy (XPS)) is used to unravel the heterogeneity of Pt degradation at inlet/outlet and land/channel locations.

2. Results and Discussion

Figure 2 shows polarization curves for four MEAs during the AST. Over the course of 30 000 cycles (≈50 h) all four MEAs showed potential loss that indicates that degradation is taking place. Comparing the polarization curves for beginning of life (BOL) and end of life (EOL) for four MEAs a clear trend emerges, where higher potential loss at medium and high current densities is observed for MEAs cycled in N_2 compared to those in air. Over the course of 30 000 AST cycles, N_2 Wet MEA had the largest polarization loss, which amounted to 0.2 V at 0.8 A cm^{-2}. For all four MEAs, the polarization curves at the BOL and after 1000 cycles either showed minimal difference (N_2 Wet), showed improved performance after 1000 cycles (Air Dry), or did not show any differences (N_2 Dry and Air Wet). 1000 AST cycles translate to 1.67 h of testing. The minimal improvement or no change of polarization during this 1.67 h. can be attributed to additional cell conditioning. Previous study has shown that for Pt/C (low surface area) the mass activity improves during first three voltage recovery cycles.[59] For the Air Dry MEA OCV of 0.95 V was observed at the BOL which decreased to, 0.94, 0.93 at 15 000 and 30 000 cycles respectively. The OCV reported here is collected after voltage recovery, as shown by Schematic S1, Supporting Information. But during the AST cycling in air environment, it was observed that the OCV (UPL for Air ASTs) decreased to 0.83 V (see Figure S1, Supporting Information), which is lower than 0.95 V UPL used for N_2 ASTs. The OCV decrease during the voltage cycling caused the AST to be performed at lower values of UPL, which reduced the amount of Pt being dissolved. As discussed in the Introduction section, this lower rate of degradation is due to decreased amount of PtO formed at lower UPL.[60–62] The potential loss during AST for all four MEAs from 1000 to 5000 cycles, from 5000 to 15 000 cycles and from 15 000 to 30 000 cycles can

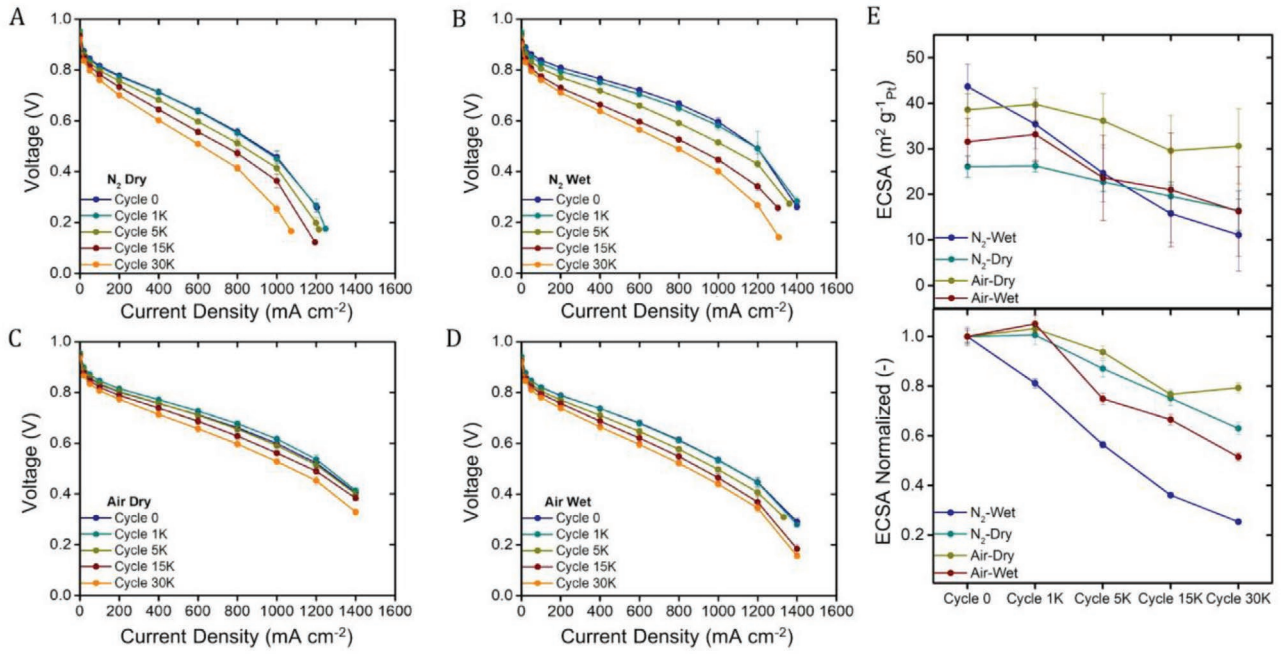

Figure 2. Polarization curves collected after 0, 1000, 5000, 15 000, and 30 000 AST cycles for a) N_2 Dry, b) N_2 Wet, c) Air Dry, and d) Air Wet. The AST conditions are reported in **Table 1**. The polarization curves are carried in H_2/Air at 80 °C, 100% RH, 150 kPa(a) backpressure, 1.5/1.8 stoichiometry anode/cathode. e) ECSA as a function of AST cycle number for N_2 Dry, N_2 Wet, Air Dry, and Air Wet MEAs (top). Normalized ECSA as a function of AST cycle number (bottom).

be approximated as equipotential within the MEA but different between MEAs. Correlation between the polarization loss and the ECSA loss is discussed in the upcoming sections.

Figure S2, Supporting Information, shows cyclic voltammetry (CV) curves for four MEAs from the BOL to 30 000 cycles. The ECSA for each experiment was calculated from the charge integrated under the H_{UPD} region with Equation 2. For all MEAs with aging the following observations were made regarding the CVs: i) the loss of the H_{UPD} region, ii) the loss of adsorbed oxide species on Pt surface, and iii) an increase in double-layer capacitive current between 0.5 and 0.65 V. The most pronounced reduction in H_{UPD} region was observed for N_2 Wet and N_2 Dry, where, together with the decrease in ECSA, we recognize a reorganization in the Pt crystal structure, as we see almost complete disappearance of the peak in the region between 0.1 and 0.15 V, generally associated with the Pt (110) direction.[63] Pt(110) has shown to be the most unstable surface using rotating disk electrode experiments, hence it is not surprising that its loss is the most pronounced in this study.[63] Figure S3, Supporting Information, shows that hydrogen cross-over and shunt resistances have not changed significantly during the AST protocols and thus are not major contributors to the MEA degradation.

Figure 2e shows the relationship of the calculated and normalized ECSA with the cycle number. Variation in the BOL ECSA is observed to be between 25 and 43 $m^2\ g^{-1}$. N_2 Dry MEA has the lowest BOL ECSA, which will be attributed to MEA-to-MEA variability during fabrication process, which also resulted in thinner catalyst layer (**Table 2**). Lower BOL double-layer capacitance also confirms this observation (Figure S4, Supporting Information). There is a slight increase in the ECSA values at 1000 cycles for the three MEAs but N_2 Wet, which can be attributed to additional cell conditioning as previously described. Such initial increase in the ECSA values has also been reported before.[64]A decrease in the ECSA is observed for all MEAs during AST cycling after 1000 cycles. N_2 Wet MEA shows the highest catalyst degradation, from 43 $m^2\ g^{-1}$ at BOL to 10 $m^2\ g^{-1}$ after 30 000 cycles. This MEA also showed the highest loss of electrochemical double-layer capacitance, which corroborates the ECSA loss (Figure S4, Supporting Information). Compared to the other three MEAs, this MEA started out with the highest ECSA and ended up with the lowest. Only 25% of the ECSA is left at the EOL. This can be attributed to the UPL that remains at 0.95 V constantly. As discussed in the

Table 1. Tafel slopes extracted from ΔV versus log($ECSA_{ratio}$) at low current density.

Condition	Tafel slope at 100 mA cm^{-2} (mV $decade^{-1}$) from BOL to EOL, where the decade refers to log($ECSA_{ratio}$)
Air dry	134
N_2 dry	195
Air wet	74
N_2 wet	90

Table 2. Catalyst layer thickness of the four MEAs acquired with cross-sectional SEM for Control sample and aged samples.

	Control	Air wet	N_2 wet	Air dry	N_2 dry
SEM-average thickness [μm]	8.13 ± 0.59	9.32 ± 0.27	8.76 ± 0.26	8.13 ± 0.48	7.45 ± 0.17

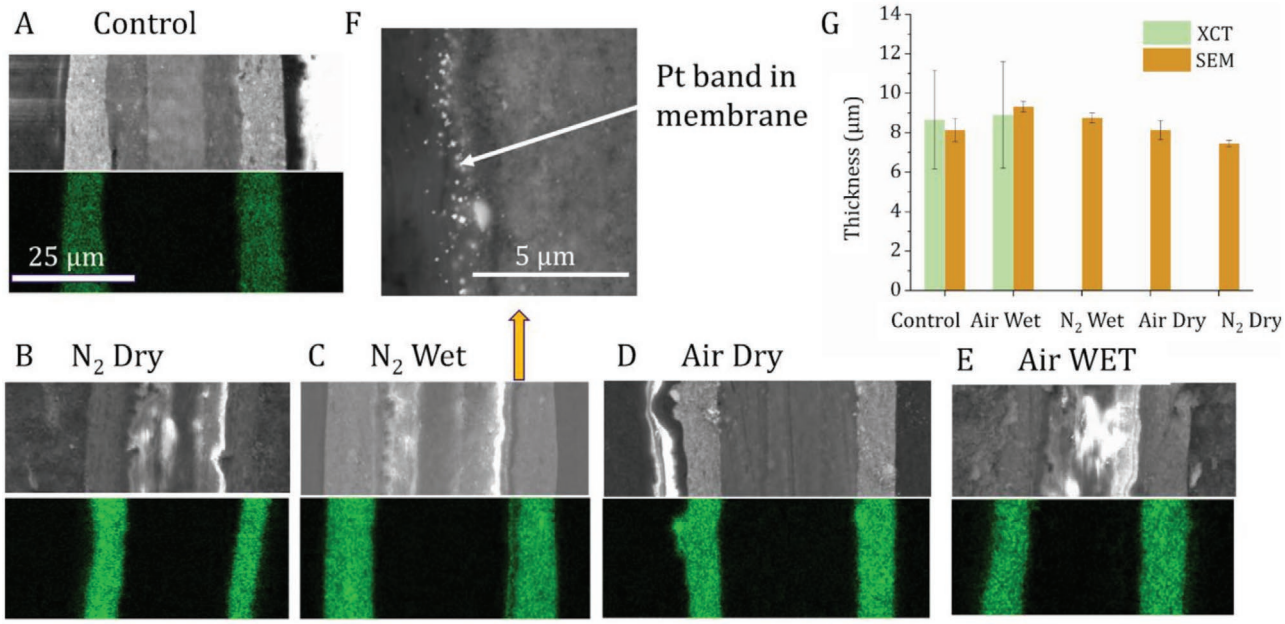

Figure 3. a–e top) Cross-sectional SEM images of the anode (left), PEM and cathode (right) catalyst layers and their respective EDS images, f) SEM image of the Pt-band formed within PEM for N_2 Wet AST, and g) the bar plot of the average thicknesses acquired from SEM and X-ray CT.

Introduction section, ECSA loss scales with the UPL. Air Dry has the least ECSA loss, and it maintains 80% of its ECSA at the EOL (from 38 $m^2\ g^{-1}$ at BOL to 32 $m^2\ g^{-1}$ at EOL). Whereas Air Wet and N_2 Dry show somewhat similar ECSA loss, maintaining 52% and 62% of the BOL ECSA and having 18 $m^2\ g^{-1}$ at the EOL. During ASTs in air environment, the UPL dropped to values below 0.9 V for both wet and dry conditions during voltage cycling. This lower UPL results in lower ECSA loss. Due to repeated oxidation and reduction of the Pt particles during AST cycling, Ostwald ripening and particle dissolution are the dominant degradation mechanisms that lead to the loss of ECSA through Pt particle size growth and Pt band formation in the- membrane.

With the loss of the ECSA, change in activation overpotential of ORR can be calculated by taking the ratio of two Tafel equations at BOL and that during aging and rearranging to obtain the following:

$$\Delta\eta = \frac{2.303RT}{\alpha F}\log\left(\frac{i_0 \cdot \mathrm{ECSA}_{\mathrm{BOL}}}{i_0 \cdot \mathrm{ECSA}_{\mathrm{Aging}}}\right) \quad (1)$$

where $\Delta\eta$ is the change in ORR overpotential from BOL to that during aging, i_0 is exchange current density that is assumed to be constant,[65] R is gas constant, T is temperature, F is Faraday's constant, and α is the symmetry coefficient that is taken to be 1 at low current densities. Only ECSA changes during aging. When $\Delta\eta$ is plotted against log ($\mathrm{ECSA}_{\mathrm{ratio}}$), a Tafel slope can be calculated and compared to the expected 70 mV $decade^{-1}$ if all the overpotential losses during aging are due to ECSA loss. Using Equation (1) Tafel slopes are calculated at a low current density of 100 mA cm^{-2} and plotted in Figure S5, Supporting Information. At 100 mA cm^{-2}, Tafel slopes of 90, 134, and 74 mV $decade^{-1}$ for N_2 Wet, Air Dry, and Air Wet MEAs were observed, respectively. Thus, N_2 Wet and Air Wet show close to expected 70 mV $decade^{-1}$ loss of overpotential, which is indicative that the polarization loss for these two cases is mainly due to the ECSA loss. For the Air Dry, the high Tafel slope value of 134 mV $decade^{-1}$ was observed, which is indicative that the polarization loss is not only due to ORR kinetics but might be affected by mass-transport or other phenomena. Overall, since the average electrode thickness was not changed during the AST cycling (see Table 2), degradation of the catalyst support due to aging is negligible.

Figure 3 shows the cross-sectional SEM images and EDS spectra for a Control sample and for the aged MEAs. The membrane is reinforced with ≈15 µm layer of PTFE in the middle. The cathode catalyst layers are observed on the right and show uniformity in thickness. Pt-band formation is identified in case of N_2 Wet conditions close to the cathode catalyst layer and PEM interface where Pt ions were reduced by crossover H_2 and deposited inside the PEM (see Figure 3f). The large loss of ECSA for N_2 Wet conditions can be ascribed to this complete loss of Pt from the cathode catalyst layer. Pt band formation in other MEAs was not sufficiently pronounced to be observed by SEM. The cathode catalyst layer thickness values are shown by Figure 3 g and tabulated in Table 2, where thickness ranged from 8.13 to 9.32 µm for three MEAs but N_2 Dry, which had a lower thickness of 7.45 µm. Furthermore, the two thicknesses from X-ray CT for Baseline and for Air Wet are also reported in Figure 3g.

Micro-XRD experiments were performed on the MEAs and 1 cm × 1 cm maps of the catalyst layer at the inlet, outlet, and middle regions are shown in **Figure 4**. The Control sample has uniform particle-size distribution of average of 3.2 nm. These particle sizes are consistent with previously reported value of 2.9 and 3.0 nm with local TEM methods,[66,67] and to the 3.3 nm estimated by XRD[68] (for TKK TEC10E50E catalyst), which has also been used in this study and the previously

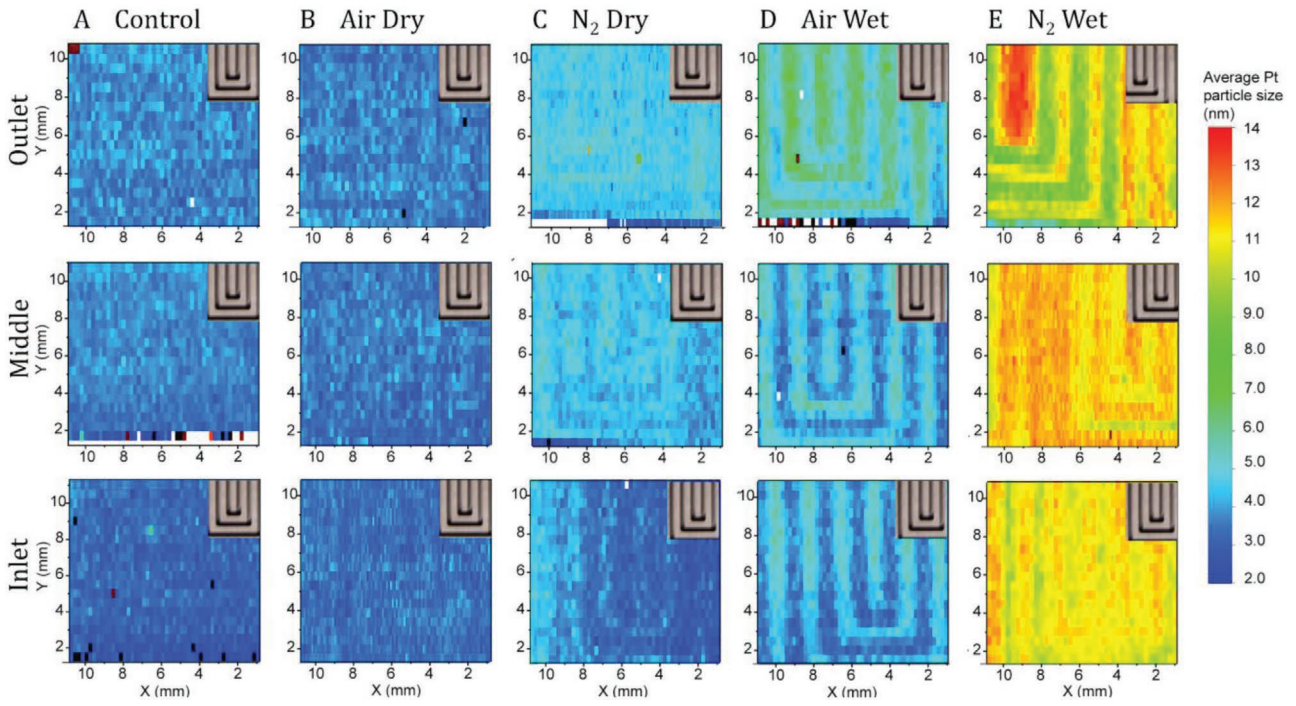

Figure 4. 1 cm × 1 cm micro XRD maps showing Pt particle size distribution in three locations (outlet, middle, and inlet) of the MEAs (a) control, post-mortem with b) air in dry condition, c) N_2 in dry condition, d) air in wet condition, and e) N_2 in wet condition. Insets show corresponding flow field geometry. Parts A and D are adopted from previous study.[51]

published study.[51] Under dry conditions (see Figure 4b) the particle size growth is not significant compared to wet conditions (see Figure 4c). For Air Dry, there is no observable particle size change compared to the Control sample. This is also the sample that maintained 80% of its ECSA at the EOL. N_2 Dry shows some Pt particle size increase under land in the middle and near the gas outlet. Mean Pt particle size observed was 4.7 nm. From the ECSA plots, N_2 Dry maintained 62% of its ECSA at the EOL. Thus, the loss of 38% of ECSA can be attributed to Ostwald ripening of particles from 3.2 to 4.7 nm via Pt dissolution. Air Wet and N_2 Wet showed the highest Pt particle size growth under land. Particularly, for Air Wet, such growth was notable at the outlet. Maximum Pt particle size observed for N_2 Wet was 14 nm, which is 4.5 times higher than the Control sample. For N_2 Wet, the difference in particle size between land and channel is significant only in the outlet region. The particle size under the channel decreased from inlet to outlet. Non-uniform humidification (inlet is more humidified compared to outlet owing to co-flow configuration and lack of produced heat and water due to absence of the ORR) is believed to be the cause for this heterogeneous particle size growth. Air Wet and N_2 Wet at EOL maintained 50% and 25% of the BOL ECSA, respectively. Air Wet had more significant change in Pt particle sizes than N_2 Wet from inlet to outlet, with prominent land to channel differences evident in all three regions. These significant changes in Air Wet are attributed to produced water mostly at the LPL (0.6 V) and subsequent heat generated due to ORR during voltage cycling. Differences in oxygen transport under land and channel lead to differences in ORR current (lower current under the land).[73] Therefore, catalyst layer located under the land is colder compared to the channel, as catalyst layer under the land generates less heat (due to lower ORR current). In addition, land conducts heat more effectively due to direct contact with the gas diffusion layer (GDL) fibers.[74] All this contributes to higher water content in the catalyst layer under land, which leads to increased PtO coverage and subsequent Pt dissolution, hence larger particle size under the land. Similarly, higher ORR current and therefore more heat is generated in the inlet region compared to outlet due to co-flow configuration of both anode and cathode gas feeds. As a result, outlet will be at a lower temperature than inlet and more humidified, which causes water accumulation in the outlet region[71,74] (more under lands). This leads to higher growth of Pt particle size in outlet region compared to inlet for air case. Previous neutron imaging studies have shown such water accumulation in air environment at the outlet.[71,72] Such inlet/outlet catalyst degradation changes in air and N_2 were observed previously[69,76] but not directly with micro XRD.

These observations are valid for relatively wide lands of 0.92 mm and one option is to design a flow-field with narrower lands. A 14-channel serpentine flow field with 0.5 mm × 0.5 mm width of land-channel (shown by Figure S6e, Supporting Information) was used to perform N_2 Wet AST and understand whether similar heterogeneous Pt degradation is observed. This flow-field also has a larger pressure drop from inlet to outlet and water will be pushed from under the lands with gas crossflow, resulting in more uniform water distribution between land and channel. Figure S6, Supporting Information, shows the Pt particle size distribution maps and associated averaged distributions, where average particle size decreased from 9.3 to 6.7 nm from the inlet to outlet. These are much smaller sizes compared to the Pt particle size observed

for 0.92 mm lands. From the 2D micro XRD map, no clear land-channel geometry was observed and unimodal Pt particle size distribution was seen. The flow-field design has a significant impact on catalyst layer degradation due to water and heat management and choosing narrow lands can minimize heterogeneous degradation of Pt catalyst.

The data from Figure 4 is summarized into a particle size distribution plot, shown in Figure S7, Supporting Information, for the gas inlet, middle, and outlet of the MEAs. The Control sample showed log-normal size distribution with mean particle sizes of 3 nm near inlet and increasing to 3.5 nm near the outlet. The inlet and outlet difference in Pt particle size is mainly due to conditioning procedure for the Control sample. For the Air Dry MEA, the mean particle size increased from 3.3 nm at the inlet to 3.6 at the outlet. For N_2 Dry the bi-modal Pt distribution is observed near the inlet with 3 and 4 nm mean Pt particle sizes, whereas for the outlet the mean increased to 4.6 nm.

From the data for Air Wet (published in the previous manuscript[51]), bi-modal Pt size distribution is observed, with mean Pt particle size increasing from 4 nm near inlet to 5.5 nm near outlet. This increase of particle size towards the outlet in Air Wet conditions is due to water accumulation at the outlet,[71,72] as water is generated during AST. Lastly, a single log-normal sharp distribution is observed near the inlet and in the middle of the MEA for N_2 Wet, with mean Pt particle size of 12 nm. The unimodal Pt distribution is because Pt distribution is more uniform under land and channel, as observed in Figure 4. But, near the outlet, bimodal distribution is observed again, due to smaller particle size under channel and larger particle size under land, with mean Pt particle sizes of 9.5 and 11.5 nm. Ostwald ripening is more pronounced for inhomogeneous particle size distribution, as smaller particles within nanometer distance to larger particles will dissolve and redeposit onto the larger particles. Here, it is important to emphasize that locally (under land or under channel) a unimodal distribution is observed and only when land and channel distributions are overlayed, they become bimodal.

The XPS survey spectra results are shown in Figure S8, Supporting Information, with the corresponding data listed in Table S1, Supporting Information, and additional discussion are provided in the SM. The high-resolution Pt 4f spectra in **Figure 5** reveals the surface composition of the platinum catalyst, comprised of reduced metallic platinum (Pt^0) and oxidized states of platinum: "surface oxidized platinum" (Pt^{2+}), usually associated with the presence of surface platinum oxide (PtO), and "edge oxidized platinum" (Pt^{4+}) usually associated with the PtO_2 represented at nanoscale by "edge oxide". XPS observations suggest that N_2 Wet MEA sample has the highest relative Pt^0 atomic concentration ≈56% and Air Wet is the 2nd highest, of about 48%, while the one of Control MEA sample shows only ≈44% (all concentrations are based on relative participation of the given moiety in the surface presence of the total chemical species). Higher content of metallic Pt^0 can be attributed to

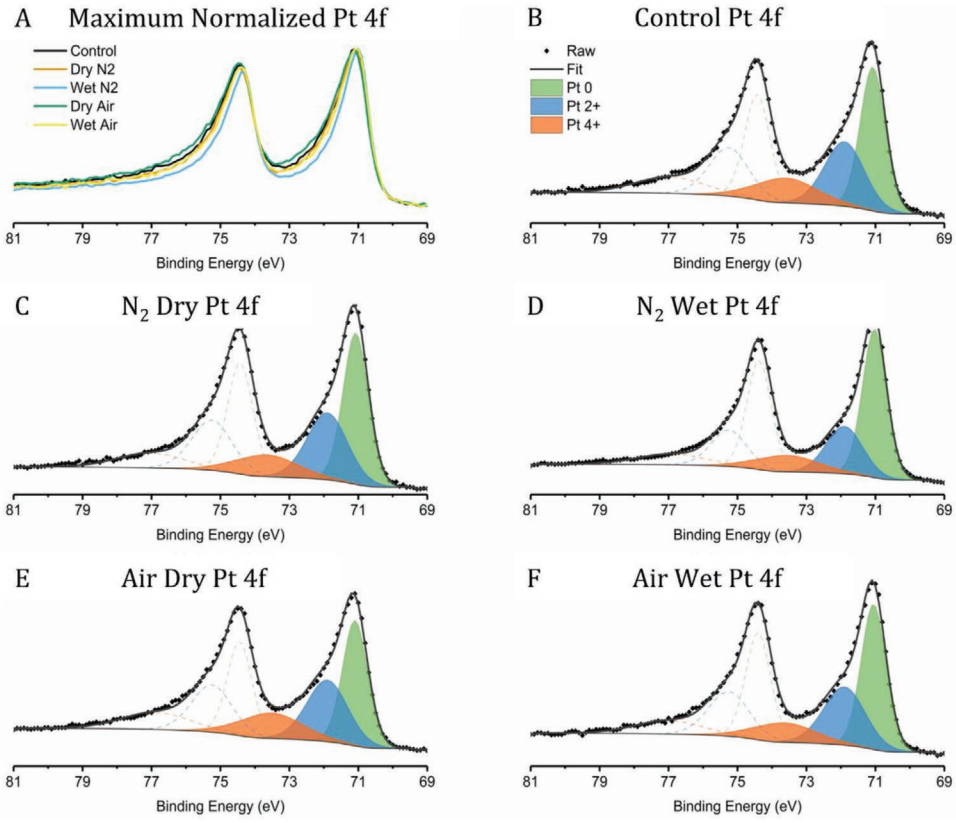

Figure 5. Curve fitted high-resolution Pt 4f of five MEA: a) Overlapped spectra with the maximum intensities of Pt 4f 7/2 normalized to 1 (a.u.); b) Control; c) N_2 Dry; d) N_2 Wet; e) Air Dry; f) Air Wet.

larger nanoparticle size. In such larger particles, a substantial portion of platinum atoms would be located inside the nanoparticle and thus will not contribute to electrocatalytic activity. On the other hand, the relative atomic concentrations of "edge" Pt^{4+} are found to be 19.4%, 17.4%, 16.0%, 20.9%, and 18.4% for Control, N_2 Dry, N_2 Wet, Air Dry, and Air Wet, respectively. In contrast with Pt^0, larger Pt nanoparticle size leads to smaller surface area and hence lower edge Pt. In general, the high-resolution Pt 4f XPS spectra are consistent with the Pt size distributions observed by microscopy and estimated by XRD. XPS spectra corroborates also with the direct observations of "Pt band" formation and Pt nanoparticles clustering in cross-section SEM and micro-XRD described above, confirming that N_2 Wet sample MEA registers severe platinum dissolution and re-agglomeration.

Specific hypothesis on the Nafion ionomer redistribution can be made from the analysis of the relative intensities change in component structure of the high-resolution C 1s spectra provided in Figure S9a and Table S2, Supporting Information, in SM. It should be noted that sp^2 carbon species (often termed "graphitic") is the main chemical state of the (element) carbon in the carbonaceous support but is entirely absent in the chemical structure of Nafion ionomer, where all the carbon is in sp^3 state. The relative atomic concentration of sp^2 carbon is ≈32% for Control and Air Dry, it elevates to about 36% for N_2 Wet and Air Wet, and as high as 41% for N_2 Dry MEA sample. The high sp^2 concentration in the N_2 Dry sample is consistent with the microscopy survey result indicating that it has the least uniform (most heterogeneous) ionomer distribution, concurrent with the observation of highest "exposed" carbonaceous support for that sample from XPS. Another interesting spectral XPS segment is the carbon-fluorine region ranging from 290–296 eV binding energy (the higher the BE is, the more F atoms are bonded with the C). Considering the Nafion chemical structure one can conclude that C—F moiety is associated solely with the sulfonate group of the ionomer, $C—F_2$ is the main building block of the Nafion polymer backbone and $C—F_3$ is the ionomer backbone terminal. Thus, the ratios between such moieties present in the spectra of MEA samples could indicate the levels of heterogeneity and interactivity of these components of the Nafion chain. We can see that the ratio of $C—F/C—F_2$ is calculated to be 1.17–0.84 for Control, 1.46–0.47 for N_2 Dry, 1.62–0.79 for N_2 Wet, 1.43–1.10 for Air Dry, and 1.41–0.93 for Air Wet. Higher ratio values for N_2 Dry and N_2 Wet imply that they have most heterogeneous sulfonate distributions, which is consistent with lower C/F ratios in survey spectra. The reason why N_2 Dry has the highest deviation in both C/F ratio (in the survey XPS spectra) and $C—F/C—F_2$ ratios (in the high-resolution C 1s spectra) is probably because the sulfonate ionomer group is hydrophilic and has less mobility at lower humidity adding a surface/chemical component to the explanation of the drying phenomena and associated with it structural changes at hierarchy of scales.

Figure S10, Supporting Information, shows the X-ray computed tomography volume-rendered images of the Control MEA (Figure S10a, Supporting Information) and the MEA with AST cycling in Air Wet conditions (Figure S10b, Supporting Information). These images reveal the woven structure of the catalyst layer. After aging some of the catalyst coated membrane is swollen into a crack in a microporous layer (MPL) (Figure S10b, Supporting Information). As it is shown in **Table 3** the catalyst layer thickness remains approximately unchanged after the AST, the result was also confirmed via the X-ray CT data, where through comparing Figure S10c,d, Supporting Information, it is seen that the thickness of the catalyst layer remains unchanged after the AST. The inhomogeneity in catalyst layer thickness is mainly due to it being woven.

Table 3. RH, gas type, and gas flow rates of different MEAs used in the AST study.

MEA name	AST RH (%)	Gas used during AST	Gas flow rate, anode/cathode [sccm]
N_2 dry	40	N_2	200/200
N_2 wet	100	N_2	200/200
Air dry	40	Air	210/830
Air wet	100	Air	210/830

To understand whether Pt loading distribution is correlated to Pt particle size distribution, or whether Pt particle growth is a local phenomenon, micro XRF mapping for N_2 Wet and Air Wet MEAs at the EOL was performed. N_2 Wet and Air Wet MEAs were selected because they showed the highest Pt particles size changes between the land and channel. **Figure 6**a shows the 2 mm x 2 mm location mapped with micro XRF near the outlet. The micro XRF signal comes from both anode and cathode catalyst layers (control sample loading ≈0.6 $mg_{Pt}\ cm^{-2}$). Figure 6b shows the Pt loading distribution curves for the three MEAs. The average Pt loading decreased from 0.6 to 0.5 $mg_{Pt}\ cm^{-2}$ for both N_2 Wet and Air Wet MEAs, indicating a loss of 0.1 $mg_{Pt}\ cm^{-2}$ of Pt from the cathode catalyst layer. Such loss of Pt loading can occur due to removal of effluent water containing Pt ions from the MEA. This Pt loading loss may be higher near the outlet due to water accumulation. Similar Pt loading loss was observed in previous studies, where Pt ions were detected in effluent water.[75] No such Pt loading loss was observed for N_2 Dry AST sample as shown by Figure S11, Supporting Information. Micro XRF also maps the woven structure of the catalyst layer, where the optical image of catalyst layer is shown in Figure 6c. Optical image clearly confirms that the structure of the catalyst layer is woven with a thread pitch of 250 µm. Figure 6d shows the control sample MEA micro XRF map near the outlet. Local bare spots are observed that are primarily due to gaps in the catalyst layer weave and some manufacturing defects. Figure 6e,f show micro XRF maps of N_2 Wet and Air Wet MEAs, where no loading redistribution was observed under the land or channel. This observation confirms that the Pt particle size growth under land is a local phenomenon.

Schematic S2, Supporting Information, summarizes the land and channel differences due to Pt dissolution during N_2 Wet and Air Wet ASTs. Under the land and in N_2 Wet AST Pt particle size increases mainly due to high mobility of Pt ions and high redeposition rates. Furthermore, observed Pt-band formation within the membrane is also due to high Pt ions mobility. For N_2 Wet AST under the channel lower Pt dissolution rates are expected because of less water present in the catalyst layer under the channel. For Air Wet AST smaller Pt

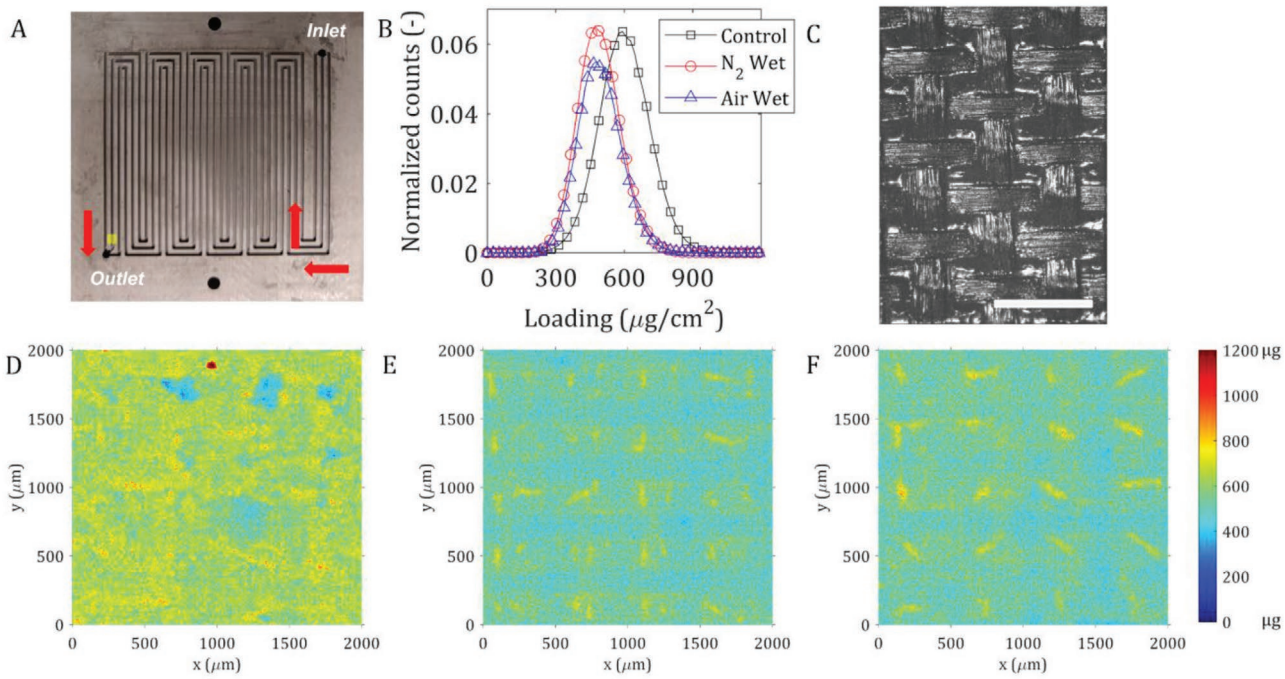

Figure 6. a) Flow-field used in the fuel cell assembly with highlighted area (near outlet) where micro XRF maps of the MEAs have been taken, b) the loading of Pt for the MEAs plotted via averaging micro XRF maps, c) the optical image of cathode catalyst layer of pristine MEA (d) control sample micro XRF map, e) N_2 Wet AST MEA micro XRF map and, f) Air Wet AST MEA micro XRF map. The size of the scale bar in (c) is 1 mm.

particle size is observed under land compared to N_2 Wet AST which can be primarily attributed to the decreasing UPL, due to dropping OCV during voltage cycling. Fewer Pt^{2+} ions are observed due to lower amount of PtO formation at decreasing UPL. Also, under these AST conditions, no Pt band formation was observed in the membrane. For Air Wet AST the Pt particle size under channel is smaller, as there is less water and lower UPL during cycling.

3. Conclusion

In this study, four MEAs were tested under different RH and gas environments using standard DOE AST protocols (voltage cycling from 0.6 to 0.95 V/OCV for 30 000 cycles) and investigated for heterogeneous catalyst degradation. The ASTs conducted were under 40% or 100% RH and in H_2/Air or H_2/N_2 environment, termed here as Air Dry, Air Wet or N_2 Dry, and N_2 Wet. For H_2/Air experiments the UPL during AST was limited by the cell OCV, which dropped as low as 0.87 V during cycling. Polarization curves showed potential loss in all the regions: activation, ohmic, and mass-transport from 1000 cycles to 30 000 cycles. CV plots showed that different Pt facets disappear at different rates (Pt (110) had highest dissolution rate) in the H_{UPD} region during cycling. Largest ECSA loss was observed for N_2 Wet, then Air Wet, N_2 Dry, and Air Dry. Tafel slopes were calculated from potential loss at BOL and during aging versus log ($ECSA_{ratio}$) at 100 mA cm^{-2} indicating that the loss in polarization for MEAs in wet conditions is mainly due to ECSA loss (≈70 mV dec^{-1} Tafel slope), whereas for dry conditions there are additional losses in polarization that cannot be explained by the ECSA loss alone.

Cross-sectional SEM, X-ray CT, and EDS showed that the catalyst layer thickness remained approximately unchanged during aging. Optical imaging and micro-X-ray CT showed that catalyst layers have woven structure. Micro XRD corroborated the ECSA loss, showing largest Pt particle size (≈14 nm) for N_2 Wet AST, second largest for Air Wet AST (≈7 nm), and smaller for N_2 and Air Dry AST (≈4–5 nm). The difference in absolute mean Pt particle size at the EOL between N_2 and air environment is due to the difference in the UPL during voltage cycling. UPL for air environment AST is OCV, which decreases during cycling, reducing PtO coverage and decreasing Pt dissolution rate during cathodic voltage sweep. Heterogeneity of catalyst degradation under land and channel is prominent in Air Wet AST due to produced water mostly at the LPL (≈0.6 V), which exacerbates the difference in thermal management of land and channel. Higher water content in catalyst layer under land increases PtO coverage and subsequently promotes Pt ion formation and mobility. Co-flow configuration of humidified gases causes water accumulation in the outlet region, which leads to heterogeneous particle size growth between inlet and outlet. The XPS study showed that relative Pt^0 atomic concentration increased in a sequence N_2 Wet, Air Wet, Dry ASTs, and Control. Higher metallic Pt content is due to larger nanoparticle size, as Pt^0 is located inside the nanoparticle. The micro XRF analysis confirmed that Pt particle size growth is a local phenomenon, as Pt loading does not follow a land-channel pattern. The analysis also confirms loss of Pt from the cathode catalyst layer.

For durable operation of PEFC under dynamic load and homogeneous catalyst degradation, it is desirable to minimize the land area to reduce relatively cold locations (under land) in

the catalyst layer. Flow-field with 0.5 mm width lands showed homogeneous catalyst degradation with no Pt particle size differences due to land-channel geometry. Furthermore, operating in a counter-flow or using alternative gas flow-field configuration can help reduce inlet-outlet degradation heterogeneity. Lastly, designing a dynamic load cycle with lower UPL by using system-level control can reduce Pt particle size growth due to Ostwald ripening. Overall, for improved catalyst layer durability, it is desirable to operate at sub humidified conditions due to reduced Pt ion migration in ionomer, which is a function of water content. Thus, higher temperature operation can help keep lower RH in the stack but at the same time may contribute to other component (non-catalyst) degradation, therefore, careful optimization is needed.

4. Experimental Section

Materials and Methods: Pt/C-based catalyst coated membranes were purchased from Ion Power Inc., New Castle, Delaware, with an active area of 25 cm^2 and loading of 0.3 $mg_{Pt}cm^{-2}$ and ionomer to carbon (I/C) ratio of 1 on both anode and cathode. The catalyst-coated membranes contained Nafion XL reinforced membrane of thickness 27.5 µm. A non-woven carbon paper, Sigracet 29 BC, with 5 wt % PTFE treatment and hydrophobic MPL was used as GDL. The total thickness of the GDL was reported by the manufacturer as 235 µm.

Testing Equipment: Fuel cell fixture hardware from Scribner Associates with POCO graphite 3X serpentine flow field (0.92 mm/0.79 mm width lands/channels) was used in co-flow configuration. Hard-stop PTFE-coated fiberglass gaskets (150 µm thickness) and PTFE gaskets (27.5 µm thickness) were used to achieve GDL compression of 22%. 13.5 Nm torque was used during the cell assembly. ASTs, polarization curves, and mass activity measurements were all performed using the 850e Fuel Cell Test Stand (Scribner Associates, Connecticut, USA) with maximum current load of 100 A. CV, LSV, and EIS were measured using VSP-BioLogic potentiostat (potential resolution of 5 µV and maximum current of 4 A).

AST Protocols: Four square wave ASTs were conducted. The conditions for ASTs were either H_2/N_2 or H_2/Air on anode/cathode both in 40% and 100% RH. The ASTs were conducted with potential cycling from 0.6 to 0.95 V in N_2 on cathode, or 0.6 to 0.95 V or OCV, if OCV <0.95 V for air gas on cathode with a dwell time of 3 s at each potential for 30 000 cycles, resulting in a total (AST only) time of 50 h. A schematic of the AST single cycle in N_2 and air is shown in Schematic S1a,b, Supporting Information. The AST was performed at atmospheric pressure and in H_2/air (anode/cathode) and H_2/N_2 environments at 100% and 40% RH with gas flow rates of 210 sccm/830 sccm (anode/cathode) for H_2/Air and 200 sccm/200 sccm for H_2/N_2. For the AST performed in air, the OCV decreased with the cycle number and for this reason, the UPL was reduced (see Figure S1, Supporting Information). The OCV was partially recovered during a voltage recovery protocol. Flow Rates were calculated for stoichiometric ratio of 1.2/2 (anode/cathode) assuming maximum current density of 1 A cm^{-2} at 0.6 V. During the AST, each MEA was characterized at stages of 0, 1000, 5000, 15 000, and 30 000 cycles. Schematic S1b, Supporting Information, lists the summary of all the ASTs and characterization experiments. Table 3 shows the four aging tests selected in this study and the naming convention used in this work.

Electrochemical Characterization: CV measurements were conducted with potential sweep from 0.095 to 0.80 V at a scan rate of 20 mV s^{-1}. LSVs were used to measure H_2 cross-over and were conducted from 0.05 to 0.80 V at a scan rate of 1 mV s^{-1}. EIS was done from 10 kHz to 0.01 Hz at 0 V versus OCV with 5 points per decade. All the previously mentioned tests were performed in H_2/N_2 environment with 200 sccm/300 sccm flow rates at anode/cathode, with 100% RH at atmospheric pressure. Polarization curves were generated by holding the cell at constant currents for 3 min and measuring the corresponding voltage values with six points in the activation region. Voltage values were averaged over these 3 min for both forward and backward scans. The test was performed at 150 kPa(a) backpressure with a stoichiometry of 1.5/1.8 in H_2/Air environment (anode/cathode) in 100% RH according to the FCTT polarization protocol. The polarization curves were preceded with a voltage recovery protocol, followed by holding the cell current density at 0.60 A cm^{-2}, at 80 °C, 100% RH, and with stoichiometry of 1.2/2.0 to ensure the polarization data was collected at the same starting conditions for all of the MEAs. The BOL data was achieved by performing a cell break-in procedure on a fresh MEA which consisted of potential holds of 30 s at 0.80, 0.60, and 0.30 V respectively until constant current was achieved. Mass activity measurements were only done at the BOL and at the EOL by holding the cell potential at 0.90 V for 15 min, measuring the corresponding current in H_2/O_2 environment at high flow gas flow rates of 1000 sccm/2000 sccm and 150 kPa(a) backpressure.

ECSA Calculation: The ECSA was calculated using the standard hydrogen underpotential deposition (H_{UPD}) region, where the area under the H_{UPD} region of the CV, was integrated to acquire the ECSA:

$$\text{ECSA} = \frac{i \times V}{L \times \upsilon \times 210} \tag{2}$$

where, the nominator represents the area of the H_{UPD} region in the CV, L is the loading of the electrocatalyst, 210 µCcm^{-2} is the unit charge and υ is the scan rate under which the CVs were performed.

Post-Mortem Analysis: Cross-sectional scanning electron microscopy (SEM) was performed to identify degradation of Pt nanoparticles and to identify morphological changes on the catalyst layer due to degradation. The following procedure was followed to obtain sample cross-sections from the SEM. First, an area of about 1 cm × 1 cm in the middle of the MEA was cut from the MEA, which was then sandwiched between stainless steel or glass plate to keep flat. The assembly was then mounted in epoxy and sectioned to expose the cross-section. Multiple polishing paper was used to polish the cross-section with finish progressively increasing from 320 grit to 1200 grit. The polished cross-section was imaged in a JOEL-7200F field emission SEM, equipped with an Oxford Instruments X-MaxN EDS detector. Catalyst layer thickness measurement was carried out using ImageJ. Multiple measurements were taken at various locations across the entire 1 cm length of the cross-section.

Micro X-Ray Diffraction: Post-mortem synchrotron X-ray micro-diffraction mapping was conducted at Beamline 12.3.2 of the Advanced Light Source (ALS) at Lawrence Berkeley National Laboratory (LBNL). A 10 keV monochromatic X-ray beam was focused to ≈2 × 5 μm^2 by Kirkpatrick–Baez mirrors. The degraded MEA disassembled from testing hardware was mounted on an x–y scan stage and tilted 25° relative to the incident beam. Diffraction images were recorded in reflection mode with a 2D Pilatus-1 M detector mounted at 60° to the incoming X-ray, approximately 150 mm away from the probe spot. Exposure time at each position was 10 s. Calibrations for distance, center channel position, and tilt of the detector were performed based on a powder pattern obtained from a reference Al_2O_3 particles taken at the same geometry. For mapping/imaging of the 1 cm ×1 cm area of each MEA sample, a scan of 50 × 20 points was performed with a step size of 200 µm on the x-axis and 500 µm on the y-axis. Finer 200 µm step size in x-axis was adopted to resolve the flow field channel (≈0.78 mm) and land (≈0.92 mm). The X-ray scan diffraction data was then processed by XMAS.[52] Diffraction rings were integrated along the azimuthal direction and the peak width was determined by fitting a 2D Lorentzian function with an angular resolution of ≈0.02°. Instrumental broadening was estimated using large Al_2O_3 crystals powder in the exact same detector configuration. The estimated Pt particle size is an average from both cathode and anode catalyst for each measured location since the synchrotron X-ray penetrates both cathode and anode. In the measurement, change of Pt particle size before and after AST was dominated by the cathode Pt catalyst particle size increase, as minimal particle size growth occurred

on the anode side, when the anode was fixed at 0.0 V versus S.H.E in pure H_2 environment during AST.

Micro XRF: Post-mortem micro XRF mapping was performed using the Horiba XGT-9000 XRF microscope. X-ray energy was set to 50 keV and 10 µm capillary was used to map an area of 2000 µm × 2000 µm (1024 px × 1024 px) of the sample. The x-ray penetrates both anode and the cathode catalyst layer and thus the net loading measurement was from both sides. 2D colormaps were generated in MATLAB using mapped fluorescence images from the microscope. Average loading was quantified for each map using a calibration curve generated from 10 µm capillary maps of calibration samples with known Pt loading. L alpha peak of Pt was used for Pt loading quantification. The average loading for each sample was reconfirmed by collecting spectrum using 1.2 mm capillary at multiple spots.

X-Ray CT: Ex situ X-ray computed tomography (CT) of MEAs was performed at Beamline 8.3.2 at ALS synchrotron at LBNL, Berkeley, CA. Monochromatic X-rays with 25 keV energy were selected. 50 µm LuAg:Ce scintillator, 10× lenses, and sCMOS PCO Edge camera were used to produce an image with 0.65 µm pix^{-1}. 200 ms exposure time was used with 1300 images collected per scan. To create the X-ray CT images, a 3D image stack was reconstructed using 2D radiographs collected from 0 to 180° rotation. The reconstructions and phase retrieval were performed using the Gridrec algorithm[53,54] with open-source TomoPy.[55] The reconstruction parameters and details were described previously.[56,57] Image processing and 8-bit conversion were carried out with open-source Fiji/ImageJ.[58] Dragonfly, Object Research Systems was used for 3D rendering.

X-Ray Photoelectron Spectroscopy (XPS): The XPS data were measured by Kratos AXIS Supra XPS, with a monochromatic Al Kα operating at 225 W for survey spectra and 300 W for high-resolution spectra. The survey spectra were acquired using 160 eV pass energy, 1 eV step size, 100 ms dwell time, while the high-resolution spectra were acquired using 20 eV pass energy, 0.1 eV step size, 100 ms dwell time. For each spectrum, the data were averaged by three random sample points and each sample point was averaged by specific cycles of scanning. All spectra were analyzed using CasaXPS software and fitted with 70% Gaussian/30% Lorentzian line shape.

Supporting Information

Supporting Information is available from the Wiley Online Library or from the author.

Acknowledgements

The micro-X-ray CT experiments used Beamline 8.3.2 and micro-diffraction mapping used Beamline 12.3.2 of the Advanced Light Source, which is a DOE Office of Science User Facility under contract no. DE-AC02-05CH11231. The authors thank Dr. Dilworth Parkinson for beamtime support. The X-ray CT volume-rendering data for this paper was generated using Dragonfly software, Version 3.6 for Windows. Object Research Systems (ORS) Inc, Montreal, Canada, 2018; software available at http://www.theobjects.com/dragonfly.

Conflict of Interest

The authors declare no conflict of interest.

Author Contributions

K.K. and M.R.T. contributed equally to this work. K.K., M.R.T., and A.P. conducted fuel cell experiments and associated data analysis. M.M.B., S.K., and K.K. conducted XRF experiments, Y.C. conducted XPS analysis and analyzed the data with P.A., N.T., and L.C. performed XRD experiments and data analysis, I.V.Z. conducted X-ray CT and image analysis, SS., N.C., C.J., and I.V.Z. helped with data analysis. All authors contributed to writing the manuscript. P.A., L.C., C.J., and I.V.Z. supervised the research.

Data Availability Statement

Research data are not shared.

Keywords

accelerated stress tests, durability, hydrogen fuel cells, material degradation, X-ray techniques

Received: June 10, 2021
Revised: July 14, 2021
Published online:

[1] G. S. Harzer, J. N. Schwämmlein, A. M. Damjanović, S. Ghosh, H. A. Gasteiger, *J. Electrochem. Soc.* **2018**, *165*, F3118.
[2] A. Kneer, J. Jankovic, D. Susac, A. Putz, N. Wagner, M. Sabharwal, M. Secanell, *J. Electrochem. Soc.* **2018**, *165*, F3241.
[3] Y. Shao, G. Yin, Y. Gao, *J. Power Sources* **2007**, *171*, 558.
[4] C. S. Gittleman, A. Kongkanand, D. Masten, W. Gu, *Curr. Opin. Electrochem.* **2019**, *18*, 81.
[5] F. T. Wagner, B. Lakshmanan, M. F. Mathias, *J. Phys. Chem. Lett.* **2010**, *1*, 2204.
[6] L. Dubau, L. Castanheira, F. Maillard, M. Chatenet, O. Lottin, G. Maranzana, J. Dillet, A. Lamibrac, J. C. Perrin, E. Moukheiber, A. Elkaddouri, G. De Moor, C. Bas, L. Flandin, N. Caqué, *Wiley Interdiscip. Rev.: Energy Environ.* **2014**, *3*, 540.
[7] L. Qu, Z. Wang, X. Guo, W. Song, F. Xie, L. He, Z. Shao, B. Yi, *J. Energy Chem.* **2019**, *35*, 95.
[8] I. V. Zenyuk, A. Lamibrac, J. Eller, D. Y. Parkinson, F. Marone, F. N. Büchi, A. Z. Weber, *J. Phys. Chem. C* **2016**, *120*, 28701.
[9] T. Yoshida, K. Kojima, *Interface Mag.* **2015**, *24*, 45.
[10] P. Gazdzicki, J. Mitzel, D. G. Sanchez, P. Aßmann, J. Sousa, T. Morawietz, R. Hiesgen, F. Häußler, J. Hunger, G. Schlumberger, et al, *ECS Trans.* **2019**, *92*, 261.
[11] S. Jomori, N. Nonoyama, T. Yoshida, *J. Power Sources* **2012**, *215*, 18.
[12] R. Borup, J. Meyers, B. Pivovar, Y. S. Kim, R. Mukundan, N. Garland, D. Myers, M. Wilson, F. Garzon, D. Wood, et al, *Chem. Rev.* **2007**, *107*, 3904.
[13] F. A. De Bruijn, V. A. T. Dam, G. J. M. Janssen, *Fuel Cells* **2008**, *8*, 3.
[14] Z. B. Wang, P. J. Zuo, X. P. Wang, J. Lou, B. Q. Yang, G. P. Yin, *J. Power Sources* **2008**, *184*, 245.
[15] P. Ren, P. Pei, Y. Li, Z. Wu, D. Chen, S. Huang, *Prog. Energy Combust. Sci.* **2020**, *80*, 100859.
[16] J. C. Meier, C. Galeano, I. Katsounaros, J. Witte, H. J. Bongard, A. A. Topalov, C. Baldizzone, S. Mezzavilla, F. Schüth, K. J. J. Mayrhofer, *Beilstein J. Nanotechnol.* **2014**, *5*, 44.
[17] A. A. Topalov, S. Cherevko, A. R. Zeradjanin, J. C. Meier, I. Katsounaros, K. J. J. Mayrhofer, *Chem. Sci.* **2014**, *5*, 631.
[18] S. Cherevko, G. P. Keeley, S. Geiger, A. R. Zeradjanin, N. Hodnik, N. Kulyk, K. J. J. Mayrhofer, *ChemElectroChem* **2015**, *2*, 1471.
[19] T. Jahnke, G. A. Futter, A. Baricci, C. Rabissi, A. Casalegno, *J. Electrochem. Soc.* **2020**, *167*, 013523.
[20] R. M. Darling, J. P. Meyers, *J. Electrochem. Soc.* **2003**, *150*, A1523.
[21] J. Marcinkoski, J. Spendelow, A. Wilson, D. Papageorgopoulos, DOE Fuel Cell Technologies Office, Record# 15015, **2015**.

[22] S. Mitsushima, S. Kawahara, K. I. Ota, N. Kamiya, *J. Electrochem. Soc.* **2007**, *154*, 153.
[23] M. Uchimura, S. Kocha, *ECS Trans.* **2007**, *11*, 1215.
[24] S. Zhang, X. Z. Yuan, J. N. C. Hin, H. Wang, K. A. Friedrich, M. Schulze, *J. Power Sources* **2009**, *194*, 588.
[25] A. Pokhrel, M. El Hannach, F. P. Orfino, M. Dutta, E. Kjeang, *J. Power Sources* **2016**, *329*, 330.
[26] I. V. Zenyuk, P. K. Das, A. Z. Weber, *J. Electrochem. Soc.* **2016**, *163*, F691.
[27] Z. Fang, A. G. Star, T. F. Fuller, *J. Electrochem. Soc.* **2019**, *166*, F709.
[28] S. Stariha, N. Macauley, B. T. Sneed, D. Langlois, K. L. More, R. Mukundan, R. L. Borup, *J. Electrochem. Soc.* **2018**, *165*, F492.
[29] A. Kneer, N. Wagner, *J. Electrochem. Soc.* **2019**, *166*, F120.
[30] P. Zihrul, I. Hartung, S. Kirsch, G. Huebner, F. Hasché, H. A. Gasteiger, *J. Electrochem. Soc.* **2016**, *163*, F492.
[31] A. Kneer, N. Wagner, C. Sadeler, A. C. Scherzer, D. Gerteisen, *J. Electrochem. Soc.* **2018**, *165*, F805.
[32] A. Kongkanand, J. M. Ziegelbauer, *J. Phys. Chem. C* **2012**, *116*, 3684.
[33] P. J. Ferreira, G. J. la O', Y. Shao-Horn, D. Morgan, R. Makharia, S. Kocha, H. A. Gasteiger, *J. Electrochem. Soc.* **2006**, *152*, A2256.
[34] E. Guilminot, A. Corcella, F. Charlot, F. Maillard, M. Chatenet, *J. Electrochem. Soc.* **2007**, *154*, B96.
[35] D. J. Myers, X. Wang, M. C. Smith, K. L. More, *J. Electrochem. Soc.* **2018**, *165*, F3178.
[36] H. Imai, K. Izumi, M. Matsumoto, Y. Kubo, K. Kato, Y. Imai, *J. Am. Chem. Soc.* **2009**, *131*, 6293.
[37] Y. Huang, J. Zhang, A. Kongkanand, F. T. Wagner, J. C. M. Li, J. Jorné, *J. Electrochem. Soc.* **2014**, *161*, F10.
[38] H. Zhang, H. Haas, J. Hu, S. Kundu, M. Davis, C. Chuy, *J. Electrochem. Soc.* **2013**, *160*, F840.
[39] X. Zhang, A. Higier, X. Zhang, H. Liu, *Energies* **2019**, *12*, 471.
[40] A. Z. Weber, J. Newman, *J. Electrochem. Soc.* **2006**, *153*, A2205.
[41] Y. Wang, K. S. Chen, J. Mishler, S. C. Cho, X. C. Adroher, *Appl. Energy* **2011**, *88*, 981.
[42] K. J. J. Mayrhofer, J. C. Meier, S. J. Ashton, G. K. H. Wiberg, F. Kraus, M. Hanzlik, M. Arenz, *Electrochem. Commun.* **2008**, *10*, 1144.
[43] T. Yoda, H. Uchida, M. Watanabe, *Electrochim. Acta* **2007**, *52*, 5997.
[44] Y. Shao, R. Kou, J. Wang, V. V. Viswanathan, J. H. Kwak, J. Liu, Y. Wang, Y. Lin, *J. Power Sources* **2008**, *185*, 280.
[45] V. A. A. S. Arico', A. Stassi, E. Modica, R. Ornelas, I. Gatto, E. Passalacqua, *ECS Trans.* **2006**, *3*, 765.
[46] J. Xie, D. L. Wood, D. M. Wayne, T. A. Zawodzinski, P. Atanassov, R. L. Borup, *J. Electrochem. Soc.* **2005**, *152*, 104.
[47] Z. Siroma, K. Ishii, K. Yasuda, M. Inaba, A. Tasaka, *J. Power Sources* **2007**, *171*, 524.
[48] K. Matsuoka, S. Sakamoto, K. Nakato, A. Hamada, Y. Itoh, *J. Power Sources* **2008**, *179*, 560.
[49] P. Yu, M. Pemberton, P. Plasse, *J. Power Sources* **2005**, *144*, 11.
[50] R. T. White, S. H. Eberhardt, Y. Singh, T. Haddow, M. Dutta, F. P. Orfino, E. Kjeang, *Sci. Rep.* **2019**, *9*, 1.
[51] L. Cheng, K. Khedekar, M. Rezaei Talarposhti, A. Perego, M. Metzger, S. Kuppan, S. Stewart, P. Atanassov, N. Tamura, N. Craig, et al, *Adv. Energy Mater.* **2020**, *10*, 2000623.
[52] G. I. R. Barabash, *Strain and Dislocation Gradients From Diffraction: Spatially-Resolved Local Structures and Defects*, Elsevier, Amsterdam **2014**.
[53] S. Vogt, S. Gleber, S. Narayanan, M. Newville, *J. Synchrotron Radiat.* **2014**, *21*, 1224.
[54] W. J. Palenstijn, J. Sijbers, *Comput. Programs* **2016**, *23*, 842.
[55] F. De Carlo, X. Xiao, C. Jacobsen, *J. Synchrotron Radiat.* **2014**, *21*, 1224.
[56] A. Serov, A. D. Shum, X. Xiao, V. De Andrade, K. Artyushkova, *Appl. Catal., B* **2018**, *237*, 1139.
[57] A. D. Shum, D. Y. Parkinson, X. Xiao, A. Z. Weber, O. S. Burheim, I. V Zenyuk, *Electrochim. Acta* **2017**, *256*, 279.
[58] C. A. Schneider, W. S. Rasband, K. W. Eliceiri, C. Instrumentation, *Nat. Methods* **2012**, *9*, 671.
[59] S. Kabir, D. J. Myers, N. Kariuki, J. Park, G. Wang, A. Baker, N. Macauley, R. Mukundan, K. L. More, K. C. Neyerlin, *ACS Appl. Mater. Interfaces* **2019**, *11*, 45016.
[60] L. Dubau, L. Castanheira, G. Berthomé, F. Maillard, *Electrochim. Acta* **2013**, *110*, 273.
[61] Y. Sugawara, T. Okayasu, A. P. Yadav, A. Nishikata, T. Tsuru, *J. Electrochem. Soc.* **2012**, *159*, F779.
[62] N. Linse, L. Gubler, G. G. Scherer, A. Wokaun, *Electrochim. Acta* **2011**, *56*, 7541.
[63] P. P. Lopes, D. Strmcnik, D. Tripkovic, J. G. Connell, V. Stamenkovic, N. M. Markovic, *ACS Catal.* **2016**, *6*, 2536.
[64] K. C. Neyerlin, R. Srivastava, C. Yu, P. Strasser, *J. Power Sources* **2009**, *186*, 261.
[65] K. C. Neyerlin, W. Gu, J. Jorne, H. A. Gasteiger, *J. Electrochem. Soc.* **2006**, *153*, A1955.
[66] E. Pizzutilo, S. Geiger, J.-P. Grote, A. Mingers, K. J. J. Mayrhofer, M. Arenz, S. Cherevko, *J. Electrochem. Soc.* **2016**, *163*, F1510.
[67] O. J. Curnick, B. G. Pollet, P. M. Mendes, *RSC Adv.* **2012**, *2*, 8368.
[68] V. A. Sethuraman, J. W. Weidner, A. T. Haug, M. Pemberton, L. V. Protsailo, *Electrochim. Acta* **2009**, *54*, 5571.
[69] Y. H. Lai, G. W. Fly, *J. Power Sources* **2015**, *274*, 1162.
[70] B. D. James, J. A. Kalinoski, K. N. Baum, Strategic Analysis, Inc., **2016**.
[71] A. Turhan, K. Heller, J. S. Brenizer, M. M. Mench, *J. Power Sources* **2006**, *160*, 1195
[72] T. A. Trabold, J. P. Owejan, D. L. Jacobson, M. Arif, P. R. Huffman, *Int. J. Heat Mass Transfer* **2006**, *49*, 4712
[73] I. A. Schneider, S. von Dahlen, A. Wokaun, G. G. Scherer, *J. Electrochem. Soc.* **2010**, *157*, 3.
[74] P. Satjaritanun, F. C. Cetinbas, S. Hirano, I. V. Zenyuk, R. K. Ahluwalia, S. Shimpalee, *J. Electrochem. Soc.* **2021**, *168*, 044508
[75] J. Xie, D. L. WoodIII, D. M. Wayne, T. A. Zawodzinski, P. Atanassov, R. L. Borup, *J. Electrochem. Soc.* **2005**, *152*, A104
[76] M. Chandesris, L. Guetaz, P. Schott, M. Scohy, S. Escribano, *J. Electrochem. Soc.* **2018**, *165*, F3290.